Micro X-ray Computed Tomography Image-based Two-scale Homogenisation of Ultra High Performance Fibre Reinforced Concrete

DOI:
10.1016/j.conbuildmat.2016.09.020

Document Version
Accepted author manuscript

In press by *Construction and Building Materials*

Micro X-ray Computed Tomography Image-based Two-scale Homogenisation of Ultra High Performance Fibre Reinforced Concrete

A. Qsymah[1], R. Sharma[2], Z. Yang*[3], L. Margetts[1] and P. Mummery[1]

[1] School of Mechanical, Aerospace and Civil Engineering, University of Manchester, M13 9PL, UK

[2] School of Engineering, Indian Institute of Technology, Mandi, 175005, India

[3] Centre for Low Impact Buildings, Faculty of Engineering and Computing, Coventry University, CV1 5FB, UK

Abstract A two-scale analytical-numerical homogenisation approach is developed to predict effective elastic properties of ultra high performance fibre reinforced concrete considering distribution of pore sizes acquired from 3D micro X-ray computed tomography (μXCT) images of 24.8μm resolution. In the first scale, the mortar, consisting of sand, cement paste and a large number of small pores (10-600μm), is homogenised using analytical Mori-Tanaka method with constituents' moduli from micro-indentation. In the second, μXCT images of a 20mm cube are converted to mesoscale representative volume elements for finite element homogenisation, with fibres and a small number of large pores (≥600μm) in the homogenised mortar. The resultant elastic moduli are compared favourably with experimental data. This approach accounts for a large number of pores with a wide size range yet without excessive computational cost. Effects of fibre volume fraction and orientation are investigated, demonstrating the approach's potential to optimise the material's micro-structure for desired properties.

Keywords: fibre reinforced concrete, X-ray computed tomography, image-based modelling, homogenisation, finite element, pores

1. Introduction

Ultra high performance fibre reinforced concrete (UHPFRC) or reactive powder concrete has many advantages over conventional concrete, fibre reinforced concrete (FRC) and high performance concrete, including considerably higher ductility, durability and strength (typically over 150MPa in compression and 9 MPa in tension) [1, 2]. These properties are achieved using a high cement content, low water/cement ratio (<0.2), fine silica sand (size <0.5mm), microsilica or silica fume, superplasticizer and other additives, resulting in a very dense cementitious matrix. Short (3-13mm), high strength (typically 2000MPa) steel fibres of

*Corresponding author: Prof. Z Yang, Email: ac1098@coventry.ac.uk

1-10% volume fraction are also added, leading to very high fracture energy (up to 40,000 J/m^2), little size effect in bending [3] and excellent impact and blast resistance [4-6].

Although the material has been used in many special structures and components, its wide applicability so far is limited, mainly due to relatively high material costs and lack of widely-accepted design codes [7]. This situation can be improved with a better understanding of the relationships between the material's internal structure and mechanical properties at micro-, meso- and macro-scales, so that the mix design can be optimised for desired performances yet with minimal costs.

Extensive experiments have been carried out to obtain the mechanical properties of UHPFRC [2-6, 8, 9] and to establish empirical relationships between the overall mechanical properties and the usage of constituents or phases [10, 11]. Experiments are often extensive, difficult and costly to carry out, especially if the effects of the phase distributions, volume fractions and local micro-structures are investigated.

Several homogenisation techniques, in which a heterogeneous material is replaced by an equivalent homogeneous continuum, have been proposed to evaluate the effective elastic properties of composite materials. A common method is analytical estimating of upper and lower bounds based on the volume fractions and elastic moduli of both matrix and reinforcement, for example, the Voigt's and Ruess's bounds [12] and Hashin and Shtrikman bounds [13]. The Eshelby's equivalent approach [14], based on single ellipsoidal inclusion in an infinite matrix, is widely used as a basis for more sophisticated analytical homogenisation approaches, such as the Mori-Tanaka (MT) scheme [15, 16], the self-consistent approach [17] and the generalized self-consistent scheme [18].

In recent years, having recognised that the mechanical properties of cementitious composites at macro-scale are highly dependent upon the nano/micro-structures and respective properties of individual constituents, researchers have made considerable efforts in developing multiscale models using the above analytical homogenisation techniques (mainly Mori-Tanaka scheme), in which the results obtained at small scale are up-scaled to predict the behaviour at larger scales. For example, multiscale models for estimation of elastic properties have been built for cement paste [19, 20], mortar and concrete [21-23] and UHPFRC [24]. Although simple and efficient, these analytical models (whether multiscale or not) cannot consider the complicated, realistic shapes, size gradations, and random distribution of the inclusions due to simplifications necessary for analytical derivations.

An alternative to analytical approaches is numerical homogenisation, mostly using the finite element method (FEM) capable of modelling complicated heterogeneous material

structures at different length scales. This approach allows homogenisation of macro-scale properties from numerical solutions of a representative volume element (RVE) [25]. Although widely used to study composite materials, its application to cementitious materials is limited. Recently a few two-step homogenisation approaches have been developed for FRC [26, 27], in which the inclusions (fibres and aggregates) and surrounding interfacial zone are homogenised first using Gaboczi's analytical method [28], and the homogenised inclusions are then integrated with the mortar matrix to predict overall elastic properties of FRC using numerical homogenisation. In these studies, the material's micro-structures used in the second step are generated using statistical algorithms with inclusions of simplified shapes and distributions, and little attention is paid to the effects of pores which exist intrinsically in cementitious composites. One important reason is the lack of real 3D internal micro-structures, and another is the high computational cost caused by explicit modelling of constituents in the micro-structures.

Recently, micro X-ray Computed Tomography (μXCT), a 3D imaging technique routinely used in hospitals, has become popular in characterising the internal nano-, micro- and meso-scale structures of many materials, because of its high resolution, non-destructive nature, and clear visualisation of shapes, sizes and distribution of multi-phases including pores and cracks. For example, μXCT has been used to characterise metals and alloys [29, 30], porous materials [31], snow [32], nuclear graphite [33], composites [34], asphalt mixtures [35], and concrete [36-38]. It has also been used to examine fibre reinforced composites such as glass fibre reinforced polymer [39] and carbon/carbon composites [40]. A few studies have used μXCT to characterise the structure and behaviour of FRC, e.g., on fibre orientations [41, 42], fibre spacing [43], and measurement of fracture energy [44].

This study aims at developing an accurate and efficient two-scale homogenisation approach for the prediction of elastic properties for fibre reinforced concrete such as UHPFRC. The 3D micro-structure of a 20mm UHPFRC cube with a voxel resolution of 24.8μm is obtained by μXCT scanning. Statistical analysis of the pore sizes in the μXCT images is then carried out based on which a two-scale homogenisation approach is developed. At the first scale, the mortar is considered as a three-phase material composed of cement paste (containing the hydrated CSH, un-hydrated cement clinkers, GGBS and silica fume), silica sand and a large number of small pores smaller than 600μm. The elastic properties of the cement paste and silica sand are obtained by micro-indentation tests. At the second scale, UHPFRC is modelled as a three-phase material with the homogenised mortar, steel fibres and a small number of pores larger than 600μm. A different homogenisation approach is used in

each scale: the analytical Mori-Tanaka average stress theory is used in the mortar step to avoid modelling the large number of small pores as in numerical homogenisation, while numerical homogenisation using 3D FE models transformed directly from μXCT images is used in the second scale. The developed method thus combines the efficient analytical approach and the realistic numerical approach. The steel fibres are modelled by both 3D solid elements and 1D truss elements. The effects of RVE size, volume fraction and orientation of steel fibres on the elastic moduli are also investigated.

2. Experimental studies

2.1. Materials and basic properties

The mix design of UHPFRC investigated in this study, summarised in Table 1, was developed at the University of Liverpool [2, 8, 9], where the detailed fabrication process could be found. The straight steel fibres are of 2000MPa in strength, 13mm in length and 0.2 mm in diameter with a volume fraction f_f=2%.

Table 1 Details of the UHPFRC Mix [2].

Mix content	Kg/m^3
Cement	657
Ground Granulated Blast Furnace Slag (GGBS)	418
Microsilica (Silica Fume)	119
Silica Sand (average diameter 0.27mm)	1051
Superplasticizer	40
Water	185
Steel fibre, f_f=2%	157
Total	2627

A 20mm cube was cut from one of the UHPFRC beams cast for a size-effect investigation [3] and used in this study. The basic properties of the material at 28 days from standard tests are [2]: compression strength 150.56MPa, tensile strength 9.07MPa, and Young's modulus 45.55GPa. They are 121.32MPa, 5.36MPa and 42.08GPa, respectively for the UHPC without steel fibres.

2.2 XCT scanning, segmentation and image analyses

The 20mm cube was scanned at the Henry Moseley X-ray Imaging Facility, the University of Manchester, UK, using a Nikon XTEK XTH 225kV machine with 130 kV and 110 μA intensity. The stage was rotated by 360°, resulting in 2985 2D radiographs with an angular displacement 0.1206^{o} and a pixel resolution 24.80μm. The scan took about 17 minutes. The 2D radiographs were then reconstructed into 3D absorption contrast image of the sample using the CT Pro and VG Studio software. Artificial defects such as beam hardening and ring effects were removed by post-processing. Fig.1a is a 2D μXCT image slice showing the mortar in grey, the fibres in white and the pores in black. A reconstructed 3D μXCT image is shown in Fig. 1b, where the mortar matrix is made transparent.

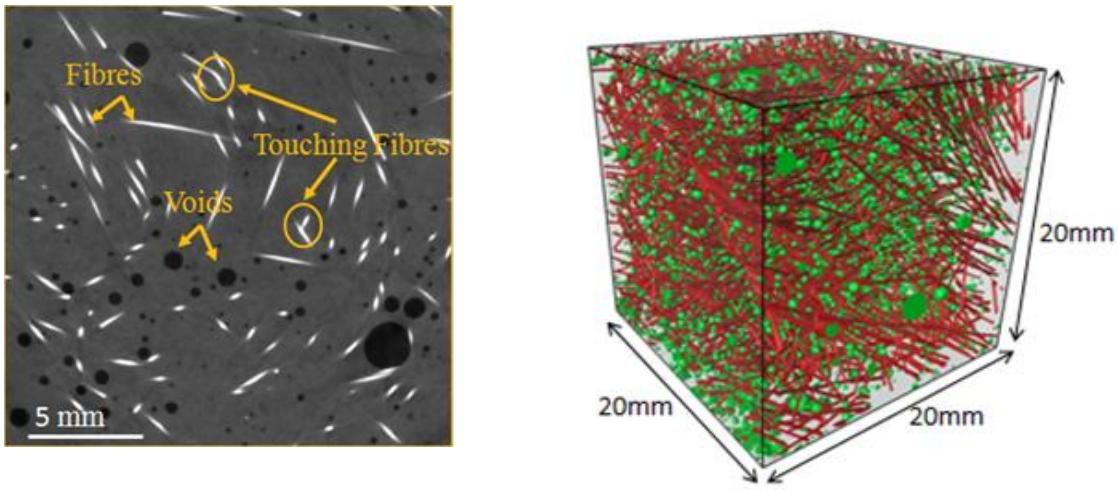

a) A 2D image slice

b) Reconstructed 3D image: fibres in red and pores in green

Fig. 1 μXCT images of UHPFRC

The 3D image was then segmented into different phases according to greyscale thresholds (0-255) using the software AVIZO (VSG, Burlington, MA). As the pore size covers a wide range (Fig. 1a), a proper selection of greyscale threshold for pores is very important. Fig .2 shows the sensitivity of pore volume fraction to the threshold. It can be seen that the pore volume fraction has a big jump at 60, indicating that some mortar matrix may be mistakenly identified as pores. This is also reflected in the segmented pore distributions in Fig .3. After careful comparison of the segmented images and the original ones, a threshold 55 was found to cover most of the pores in all μXCT images.

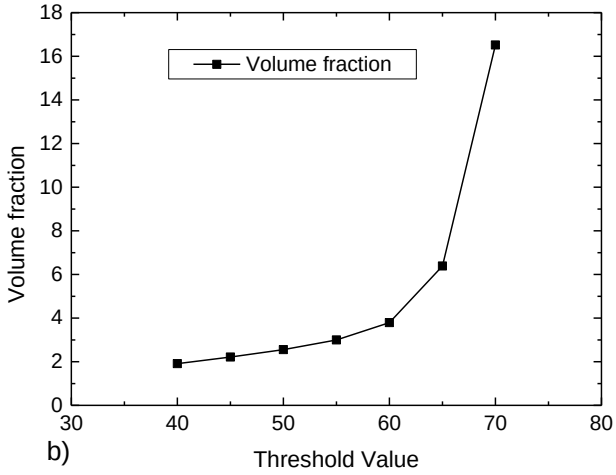

Fig. 2 Sensitivity of pore volume fraction to the greyscale threshold

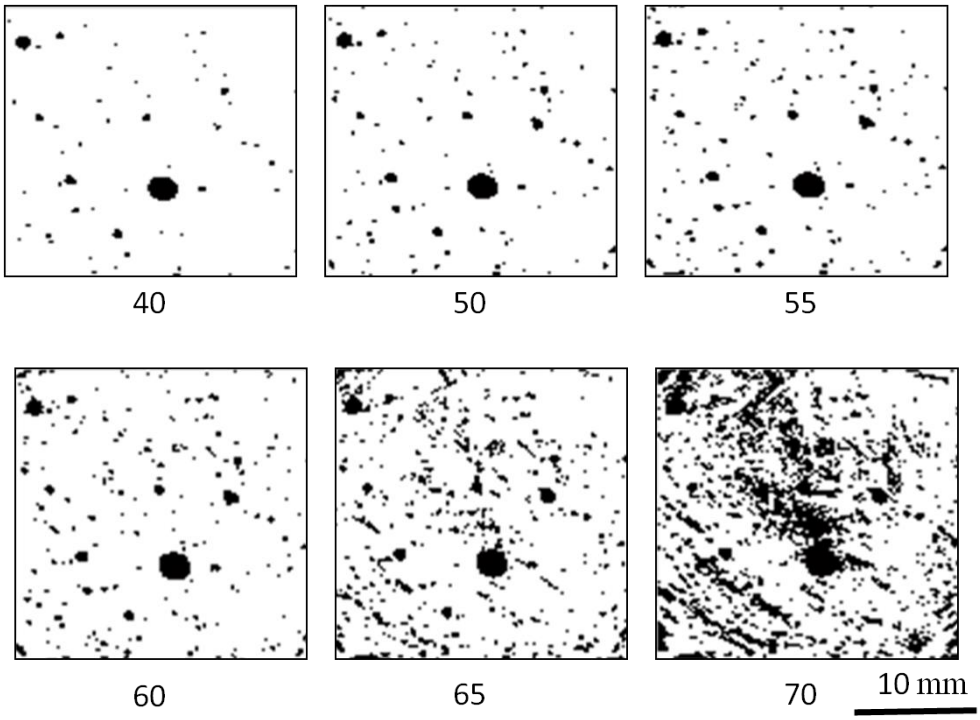

Fig .3 Pores identified using different greyscale thresholds in a 2D image slice.

Fig .4 shows the 3D image of the pores with grey value ≤ 55. The resultant pore volume fraction is 2.99%. It can be seen from Fig .4 that most of the pores are nearly spherical in shape. The volume of each pore was calculated by counting the voxels inside it, from which an equivalent diameter (d_e) was calculated assuming the pore was a sphere. The frequency histogram of d_e was then obtained and shown in Fig .5. It was found that the total number of

pores is 12311, and among them 58.5% has d_e=25-200 μm, 28.3% has d_e=200-350 μm and 13.2% has d_e=350-1400 μm, respectively. In this study, 97.7% of pores with $d_e \leq$ 600 μm are classified as small pores and 2.3% with d_e=600-1400 μm as large pores. The volume fraction for the small pores and the large pores are 1.56% and 1.43% respectively from the image analyses.

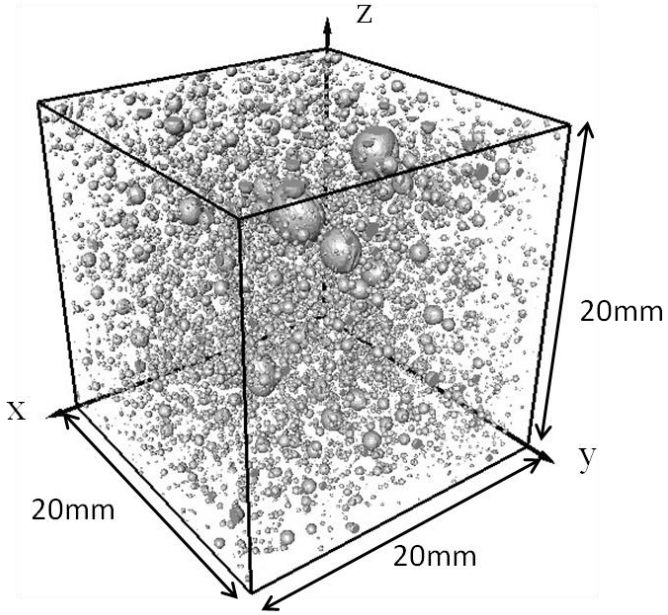

Fig .4 Segmented 3D μXCT image of pores

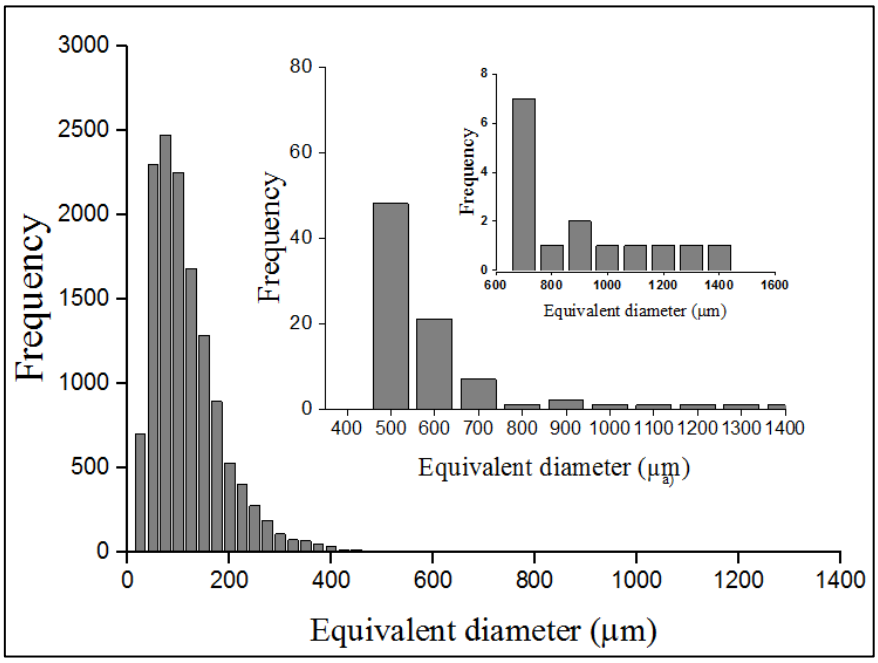

Fig .5 Frequency distribution of pores' equivalent diameters (d_e).

As a sharp distinction exists between the steel fibres and the mortar matrix (Fig .1a), a threshold 140 is easily identified for steel fibres with consideration of the fibre diameter 0.2mm. The voxels with grey values between 55 and 140 are then identified as the mortar matrix. Fig .6 shows the segmented 3D μXCT image of N=1533 fibres with grey value ≥ 140. The fibre volume fraction, which is found as f_f=3.75%, is much higher than 2% in the mix design (Table 1), indicating non-uniform distributions of fibres during casting, which is a common problem in UHPFRC specimens [45].

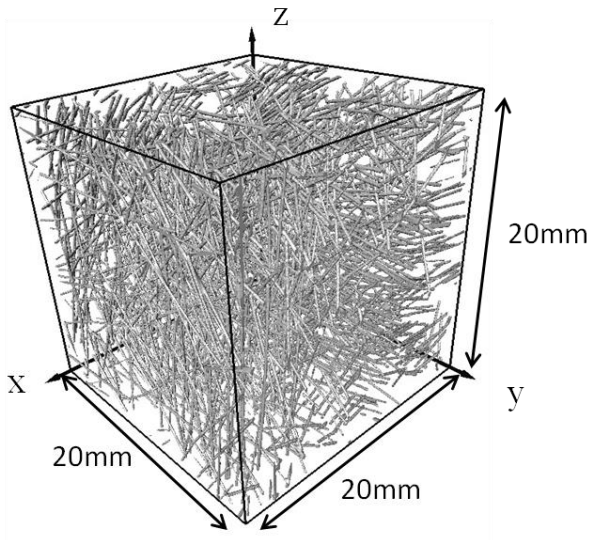

Fig .6 Segmented 3D μXCT image of steel fibres

The mechanical properties of UHPFRC are significantly dependent on fibre orientations [41, 45]. The segmented μXCT images of fibres in Fig .6 can be used to characterise the overall orientation of fibres. First, a skeletonisation algorithm developed by [46] was implemented in a Matlab code to identify one voxel-thick fibre skeleton (centreline) of each fibre. Next, the orientation angle of each fibre with respect to a global axis (*x*, *y* or *z*) was calculated from the centreline's coordinates. These angles were then used to compute an overall orientation factors η_i with respect to the considered global axis *i* by [45]

$$\eta_i = \frac{1}{N}\sum_{j=1}^{N}\left|cos\phi_{ij}\right| \quad (1)$$

where i=1,2, and 3 corresponding to *x*, *y* and *z* axes, ϕ_{ij} is the angle of j^{th} fibre centreline with respect to the axis i. From the μXCT image, the calculated η_i is 0.68, 0.42 and 0.25, respectively, indicating the majority of fibres in this specimen tend to align along the *x* axis.

2.3 Optical microscopy observations and micro-indentation tests

The mortar matrix contains silica sand particles with average diameter 0.27mm [2] as shown in Table.1. However, as the silica sand and the cement paste have similar density and thus same level of greyscale values particularly for dense mortar [47], they cannot be differentiated in the μXCT images. An optical microscopy was thus used. Fig .7 shows the detailed micro-structure of a small area (2.3×1.8mm) of the mortar matrix.

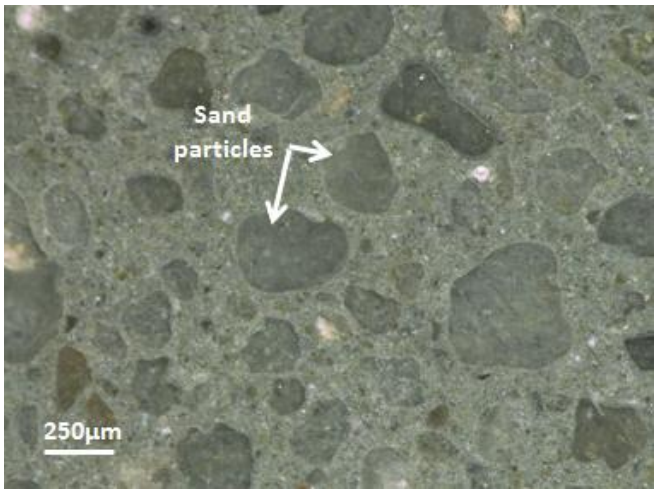

Fig .7 Optical microscopy image of mortar matrix showing sand particles.

The elastic moduli of silica sand and cement paste were measured using the micro-indentation technique. A specimen ($20\times20\times10mm^3$) was prepared by grinding and polishing its surfaces to obtain reliable and repeatable indentation measurements. A total of 150 indentations were recorded for silica sand and cement matrix using a CSM micro-indentation test machine (CSM, 2010) with Vickers indenter, using different peak forces from 0.3 N to 1.0 N. Fig .8a shows the indentation marks in the silica sand under different peak forces and Fig .8b those in the cement paste at 0.3N peak force as examples, respectively. Fig .8b shows that some indentation marks touched the steel fibres and their measurements were discarded. The load vs. penetration depth curves for each indent was recorded and used to calculate the elastic moduli using the Oliver and Pharr method [48]. Fig .9 shows some examples for 1 N peak force.

Figs .10a and b show the frequency histogram of the elastic moduli for the silica sand and the cement paste, respectively. The mean and the standard deviation are 88.61 and 14.46 GPa for the silica sand, compared with 70.00 to76.30 GPa and 13.00-15.10 GPa for quartz sand in the literature measured by nano-indentation [23, 24] and micro-indentation [22]. The obtained mean and standard deviation of elastic moduli for the cement paste is 58.33 GPa and 14.21 GPa, respectively, compared with much lower elastic moduli for normal cement paste, e.g., 22.80 GPa for w/c=0.5 [19].

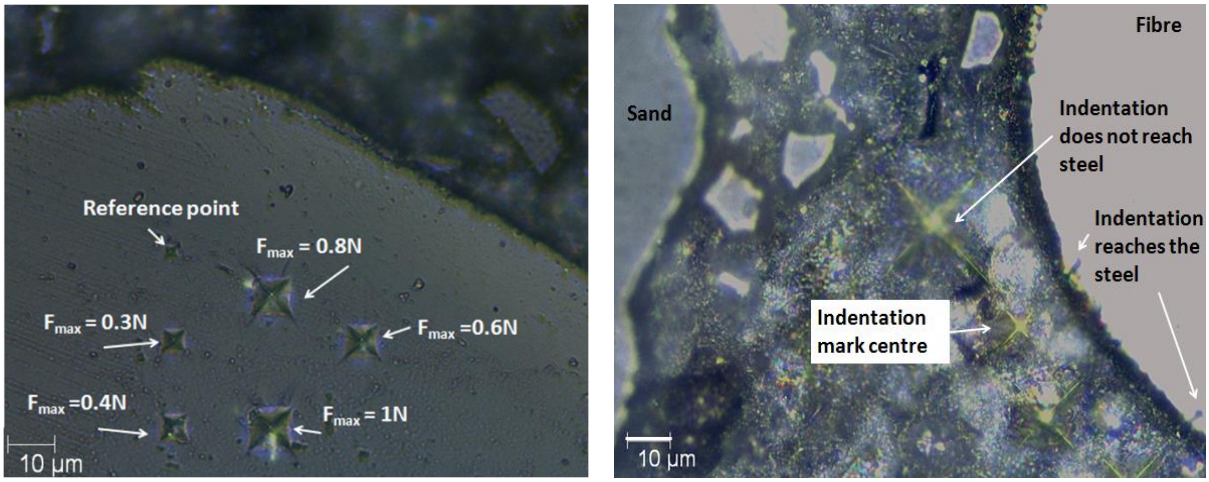

a) In a sand particle (different peak loads) b) In the cement paste (peak force 0.3N)

Fig .8 Micro-indentation marks

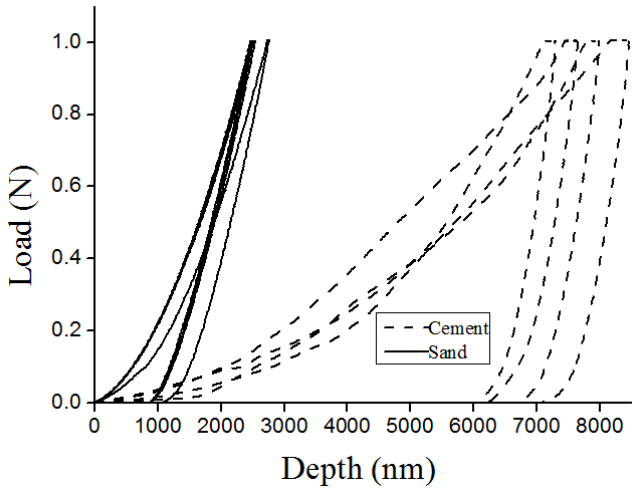

Fig .9 Load-depth curve for cement and sand for peak force 1N.

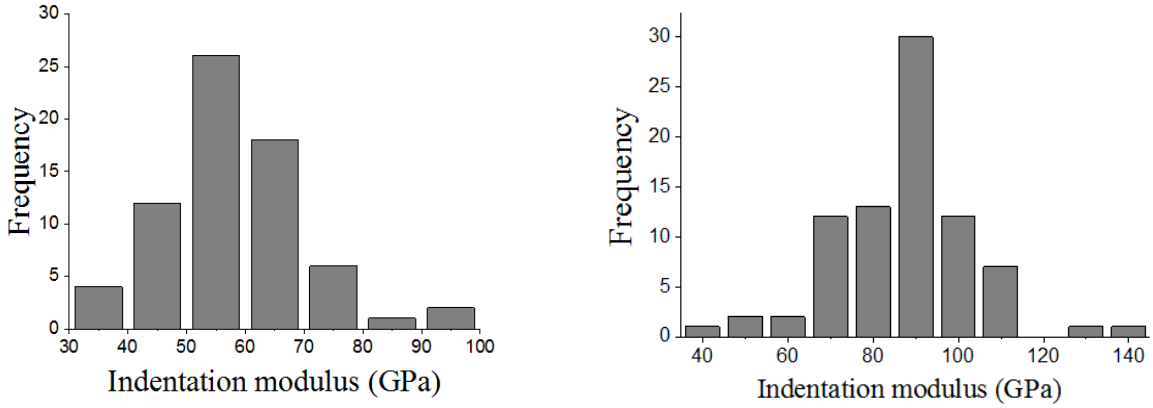

a) cement paste b) silica sand

Fig .10 Histograms of the micro-indentation measurements

3. The two-scale homogenisation approach for UHPFRC

Based on the statistical data of pore size (Fig. 5) analysed from the μXCT images and considering computational efficiency, a two-scale analytical-numerical homogenisation approach was developed to calculate the effective elastic properties of UHPFRC. It is illustrated in Fig .11 and discussed in detail as follows.

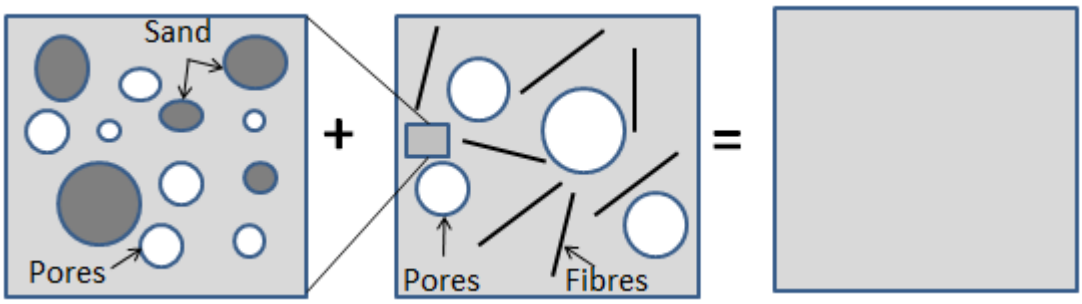

Fig .11 The two-scale analytical-numerical homogenisation approach for UHPFRC: (a) analytical homogenisation of mortar at micro-scale (cement paste + silica sand + small pores (d_e=10-600 μm); (b) numerical homogenisation at meso-scale (homogenised mortar + fibres + large pores (d_e=600-1400 μm); (c) homogenised macro-scale UHPFRC

3.1 Analytical homogenisation at the micro-mortar scale

At the mortar scale, the mortar was considered as three-phase material in which the silica sand and pores are inclusions embedded in the cement paste. The elastic properties of mortar matrix were predicted using the analytical Mori-Tanaka scheme based on classical Eshelby's solution of ellipsoidal inclusions embedded in an infinite matrix [15, 16]. In this scheme, the homogenised bulk (k_H) and shear (G_H) moduli of a composite with r number of inclusion phases can be evaluated using [23]:

$$k_H = \frac{\sum_{c=1}^{r} f_c\, k_c \left(1+\alpha_m\left(\frac{k_c}{k_m}-1\right)\right)^{-1}}{\sum_{c=1}^{r} f_c \left(1+\alpha_m\left(\frac{k_c}{k_m}-1\right)\right)^{-1}} \tag{2}$$

$$G_H = \frac{\sum_{c=1}^{r} f_c\, G_c \left(1+\beta_m\left(\frac{G_c}{G_m}-1\right)\right)^{-1}}{\sum_{c=1}^{r} f_c \left(1+\beta_m\left(\frac{G_c}{G_m}-1\right)\right)^{-1}} \tag{3}$$

with α_m and β_m defined as:

$$\alpha_m = \frac{3k_m}{3k_m + 4G_m} \tag{4}$$

$$\beta_m = \frac{6k_m + 12G_m}{15k_m + 20G_m} \tag{5}$$

where k_m and G_m are the bulk and shear moduli of matrix m, and k_c and G_c are the bulk and shear moduli of the inclusion phases c (c=1~r) respectively. The parameter $f_c = V_c/V$ is the volume fraction of the inclusion c in the volume V, such that $f_m + \sum_{c=1}^{r} f_c = 1$ and f_m is the volume fraction of the matrix.

The homogenised bulk and shear moduli are then used to evaluate the homogenised Young's modulus and Poisson's ratio using:

$$E_H = \frac{9k_H.G_H}{3k_H + G_H} \tag{6}$$

$$\nu_H = \frac{3k_H - 2G_H}{6k_H + 2G_H} \tag{7}$$

3.2 Numerical homogenisation at the meso-fibre scale

The widely-accepted computational homogenisation method [49, 50] was applied at the fibre (meso) scale to estimate the effective elastic properties of UHPFRC. In this method, six independent loading cases with suitable boundary conditions are applied on representative volume elements (RVEs), which are modelled with detailed multi-phasic constituents.

The general constitutive relation of a heterogeneous material in terms of computational homogenisation can be expressed as:

$$\langle \sigma_{ij} \rangle = C^H_{ijkl} \langle \varepsilon_{ij} \rangle \tag{8}$$

where C^H_{ijkl} is the homogenised stiffness matrix, $\langle \sigma_{ij} \rangle$ and $\langle \varepsilon_{ij} \rangle$ are the volume averaged stress and strain tensors of the RVE respectively. These average stress and strain can be obtained in terms of local elemental stresses and strains as follows:

$$\langle \sigma_{ij} \rangle = \frac{1}{|V|}\left[\int_{V_m} \sigma^m_{ij}\, dV_m + \int_{V_f} \sigma^f_{ij}\, dV_f\right] \tag{9}$$

$$\langle \varepsilon_{ij} \rangle = \frac{1}{|V|}\left[\int_{V_m} \varepsilon^m_{ij}\, dV_m + \int_{V_f} \varepsilon^f_{ij}\, dV_f\right] \tag{10}$$

where V is the volume of the RVE, V_m and V_f are the volumes of mortar and fibre phases respectively. Alternatively, the average stress and strain can be obtained from the boundaries reaction forces and displacements using [51]:

$$\langle \sigma_{ij} \rangle = \frac{1}{2|V|} \int_s \left(t_i x_j + t_j x_i \right) ds \tag{11}$$

$$\langle \varepsilon_{ij} \rangle = \frac{1}{2|V|} \int_s \left(u_i n_j + u_j n_i \right) ds \tag{12}$$

where s is the surface of the RVE, t the traction on the boundaries, x the position vector, u the displacement and n the unit normal vector.

The RVE is subjected to uni-axial tensile and shear deformation along the three axes of coordinates to determine the components of C_{ijkl}^{H}. Different boundary conditions on the RVE can be applied as long as the Hill-Mandel condition is satisfied for energy equivalence. Herein the following kinematic uniform boundary conditions (six displacement boundary conditions on the RVE boundary s) are applied [49, 52]:

$$u_i = \varepsilon_{ij}^0 . x_j , \qquad \forall\, x \in s \tag{13}$$

where i and j =1, 2 and 3 corresponding to x, y and z axes and ε_{ij}^0 are the components of a uniform applied strain.

4. Results and Discussion

4.1 Mortar scale

The analytical model (Eqs 2-7) needs the elastic moduli, Poisson's ratios and volume fractions of the involved phases as inputs. The elastic moduli of silica sand and cement paste were taken from the mean indentation measurements as E_s=88.61GPa, and E_{cm}=58.33GPa, respectively. The Poisson's ratio is 0.21 and 0.20 for the silica sand and the cement paste, respectively [24]. The volume fractions f at this scale are evaluated based on mass proportions of the mix design shown in Table 1. Knowing that the mass density of silica sand is 2652 kg/m^3 [9], its volume fraction is calculated as f_s=39.20%.

The volume fraction of pores at the mortar scale, however, is difficult to determine. Although the small pores with d_e=25-600 μm are included in this scale, the pores smaller than 25 μm that cannot be identified by the μXCT scanner must also be considered. Assuming that the mechanical effects of pores with d_e <10 μm have already been captured by the micro-indentation measurements and thus could be neglected, all the pores with d_e=10-600 μm are considered in this scale [24]. According to studies in [23, 24], the volume fraction of pores with d_e>10 μm for high performance concretes is 8.9% to 11.7%, with corresponding elastic moduli of 52.7 GPa to 34.9 GPa. It was also found that the elastic modulus of UHPFRC is approximately inversely proportionate to the porosity up to 10% [24]. As the tested UHPFRC

has E =45.5 GPa (28 days)[2], it is reasonable to infer that the porosity with d_e>10 μm is 10%. As the pores with d_e>600 μm modelled at the second scale (fibre scale) has f_p=1.43% as revealed in the XCT scan, the pores modelled at this scale has thus f_p=8.57% (10%-1.43%). Finally, the volume fraction of cement matrix at this scale is f_{cm}=1-f_p-f_s=1-39.20%-8.57%=52.23%.

The interfacial transition zone (ITZ) between the cement matrix and the inclusions (sand particles and steel fibres) in UHPFRC differs from that in ordinary concrete and normal FRC made with higher w/c ratio [24]. Testing the ITZ in UHPFRC using micro-indentation is not possible because the thickness of the ITZ (1~5 μm) [53] is very small compared with the indenter size (>10 μm), as shown in Fig .8 where most of the indentation marks at the ITZ reached the steel fibres. In addition, nano-indentation tests [24, 53] found that the ITZ in UHPFRC is as stiff as the bulk matrix. The ITZ was thus neglected in this study.

Substituting the above parameters into Eqs (2-7), the homogenised elastic properties of the mortar were calculated as E_m=57.30GPa and ν_m=0.207. The material properties at this scale are sammarized in Table.2.

Table 2. Input-output at the mortar scale.

	E (GPa)	ν [Sorelli 2008]	f(%)
Sand	88.61 (±14.46)	0.21	39.20
Cement matrix	58.33 (±14.21)	0.20	52.23
Porosity	-	-	8.57
Homogenised mortar	**57.30**	**0.207**	-

4.2 Fibre scale

4.2.1 Full 3D FE models

Five sizes of cubic RVEs, i.e., 5mm, 6.5mm, 9mm, 13 mm, and 16.5mm, cut from the segmented 3D μXCT images of the UHPFRC cube, were modelled. To investigate the effects of random distribution of internal phases, several RVEs at different regions were modelled for each size: 20 for 5mm, 10 for 6.5mm, 5 for 9mm, 3 for 13mm and 1 for 16.5mm. One RVE for each size is shown in Fig. 12. These images were converted into finite element meshes using the commercial software ScanIP (Simpleware Ltd., UK) after the pores with d_e<600μm were removed from the images in Matlab and replaced by mortar. The meshes were generated with free-meshing control in ScanIP with element size in the range 0.056~0.136mm. The mesh for a 5mm cube is shown in Fig. 13 as an example. It has 213,478

nodes and 902,522 tetrahedron elements for mortar and 231,832 elements for fibres. All the finite element analyses were conducted using ABAQUS.

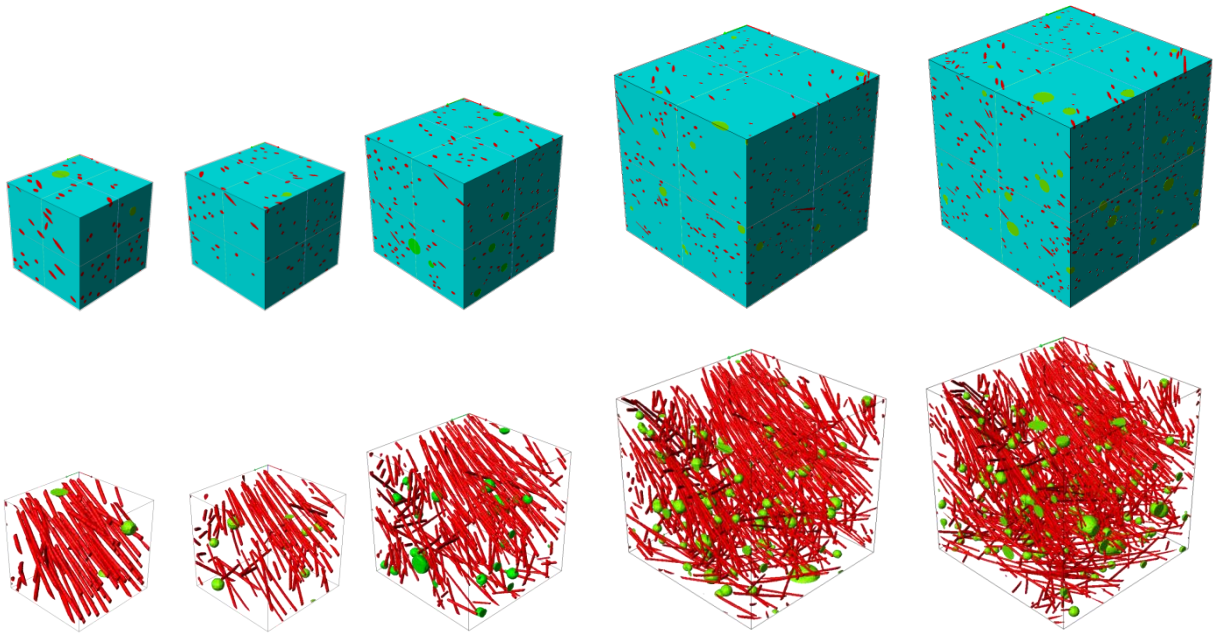

Fig .12 Example of RVEs of different sizes: from left to right: 5mm, 6.5mm, 9mm, 13mm and 16.5mm (mortar in blue, fibres in red and pores in green)

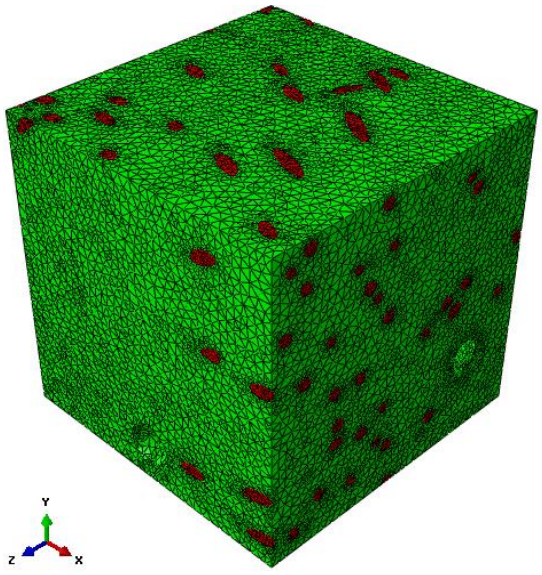

Fig .13 A finite element mesh for 5 mm RVE with steel fibres in red.

Each FE model was simulated under the six loading conditions given in Eq .13. Fig .14 shows the deformation modes with stress contours of a 9mm RVE as an example. Figs .14 a, b and c show the normal stress contours $S11$, $S22$, and $S33$ (in MPa) under unit normal strain ε_{11}, ε_{22} and ε_{33} respectively, while Figs .14 d, e and f show the shear stress contours $S12$, $S13$ and $S23$ under unit shear strain ε_{12}, ε_{13} and ε_{23} respectively. It can be seen that,

the local stresses in the mortar matrix concentrate mainly around pores as well as near 3D fibre elements. The stresses in the fibres are higher than those in the cement for all loading conditions because they are much stiffer.

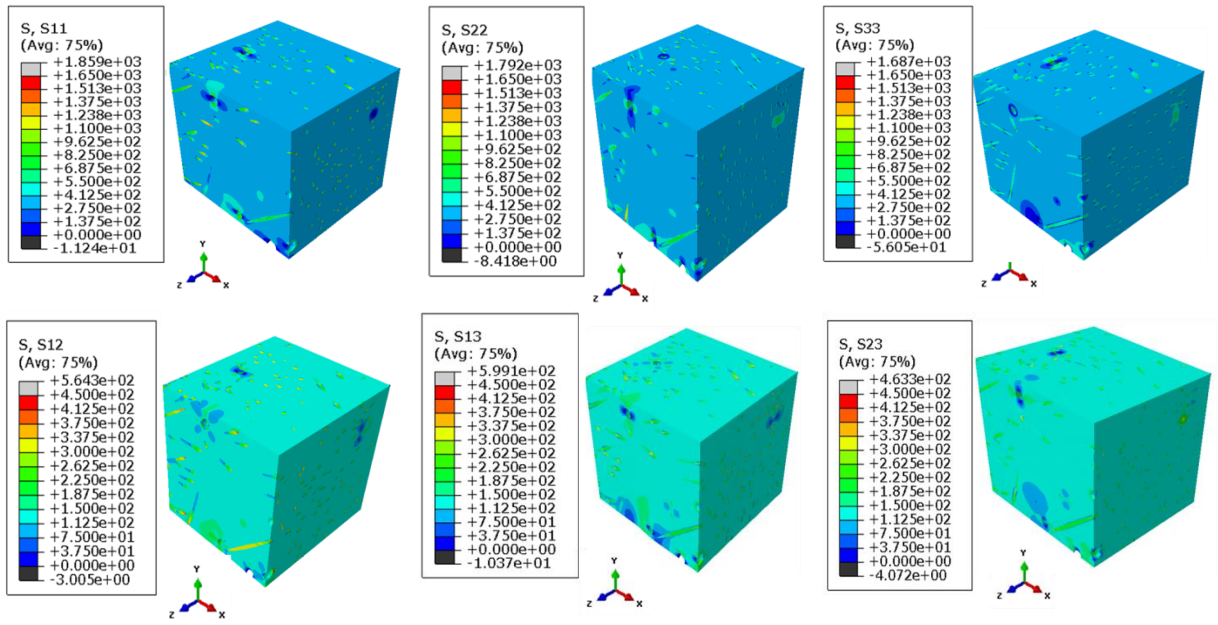

Fig .14 Stress contours under six loading cases for 9mm RVE

The homogenised stiffness coefficients were then determined using Eqs. 8-10, and Eq. 14 shows the results for a 9mm RVE as an example. The coupling terms show that extension-shear and shear-shear components were much lower than those of extension-extension and were negligible.

$$C_{ijkl}^{H} = \begin{bmatrix} 65.56 & 16.53 & 16.49 & 0.08 & 0.09 & 0.17 \\ & 64.86 & 16.31 & 0.05 & -0.01 & 0.23 \\ & & 64.36 & -0.02 & 0.10 & 0.32 \\ & \text{Symmetric} & & 24.29 & 0.30 & 0.02 \\ & & & & 24.17 & 0.01 \\ & & & & & 24.08 \end{bmatrix} \quad (14)$$

Extension- Extension

Shear- Extension

Shear- Shear

The calculated means and standard deviations for the five 9mm RVE are:

$$C_{ijkl}^{H} = \begin{bmatrix} 65.58 \pm 0.27 & 16.60 \pm 0.13 & 16.45 \pm 0.11 & 0 & 0 & 0 \\ & 65.58 \pm 0.50 & 16.33 \pm 0.10 & 0 & 0 & 0 \\ & & 64.40 \pm 0.30 & 0 & 0 & 0 \\ & \text{Symmetric} & & 24.32 \pm 0.15 & 0 & 0 \\ & & & & 24.17 \pm 0.11 & 0 \\ & & & & & 24.08 \pm 0.12 \end{bmatrix} \quad (15)$$

A cubical symmetry could be seen in Eq. 15, from which the elastic constants of the RVEs could be calculated. The elastic constants for all the RVE sizes are listed in Table 3, where the effective homogenised properties (EHP) are the volume averaged values of all the RVEs. It can be seen that the elastic moduli E_{22} and E_{33} are slightly less than E_{11} for all sizes. This is related to the orientation of fibres which tend to align with the *x* axis as explained in section 2.2 and has been observed in experiments [54].

Table 3: Engineering constants of different sizes of RVEs with associated uncertainties.

RVE size(mm)	E_{11} (GPa)	E_{22} (GPa)	E_{33} (GPa)	G_{12} (GPa)	G_{13} (GPa)	G_{23} (GPa)	ν_{12}	ν_{13}	ν_{23}
5	58.93± 1.26	58.34 ± 1.15	57.96± 1.34	24.38± 0.64	24.21± 0.60	24.11± 0.60	0.211± 0.002	0.209± 0.002	0.207± 0.001
6.5	58.67± 1.05	58.59± 0.78	57.79± 0.91	24.28± 0.39	24.12± 0.48	24.05± 0.39	0.210± 0.001	0.207± 0.002	0.208±0. 001
9	58.83± 0.22	58.15± 0.44	57.83± 0.26	24.31± 0.15	24.17± 0.12	24.08± 0.12	0.211± 0.001	0.210±0. 001	0.210±0. 002
13	59.11± 0.09	58.16 1±0.41	57.49± 0.05	24.21± 0.08	24.01± 0.03	24.12± 0.02	0.212± 0.001	0.209±0. 001	0.209±0. 001
16.5	59.83	57.32	57.57	24.26	23.99	23.85	0.208	0.210	0.208
EHP	58.97± 0.24	58.10± 0.55	57.72± 0.19	24.29± 0.06	24.10± 0.10	24.04± 0.11	0.21±0. 001	0.209±0. 001	0.208±0. 001
Finally averaged	E_H=58.26±0.64			G_H=24.14±0.13			ν_H=0.209±0.001		

The anisotropy ratio (a) of the planes is defined as

$$a = \frac{2C_{44}}{C_{11} - C_{12}} \quad (16)$$

where C_{11}, C_{12} and C_{44} are coefficients of the homogenised stiffness matrix (Eq. 8) averaged for all RVEs of the same size. The anisotropy ratio was found close to 1 (in the range of 0.965~1.013), suggesting that this UHPFRC specimen can be considered as isotropic. The final homogenised Young's modulus, shear modulus and Poisson's ratio are calculated by averaging all moduli of all RVEs as E_H=58.26±0.64GPa, G_H=24.14±0.13GPa and ν_H=0.209±0.001, respectively (also shown in Table 4).

4.2.2 3D FE Models with 1D fibres

The steel fibres were also modelled by 1D bar/truss elements to save computational cost so that fast simulations can be carried out for parametric studies. The voxels of fibres in the μXCT images were replaced by mortar. The centrelines for all fibres, obtained from the skeletonisation process in the segmentation aforementioned, were used to generate 1D truss elements in a Matlab code. They were then embedded into the homogenised mortar matrix with perfect bond. This led to considerable reduction in the degrees of freedom in the FE models. For example, using the same range of the element size as in Fig. 13, the FE model using 1D truss elements for the 5mm RVE has only 79,131 nodes and 388,195 elements in total, with only 64 truss elements for fibres.

For these models, the homogenised stiffness coefficients were determined from the reaction forces of the RVE boundaries according to the Eqs. 11-12. The results are very close to those in Table 4 (ref. Fig. 15) and the anisotropy ratio was found to be 0.971-0.986.

4.2.3 Effects of RVE size

Fig .15 plots the RVE size versus the homogenised Young's moduli (averaged by the number of RVEs for each size) and the errors for both 1D and 3D modelling of fibres. From these results, it can be concluded that 9mm is big enough to yield stable elastic modulus for both models, and thus can be regarded as representative. It can also be seen that modelling fibres using 3D or 1D elements made little difference to the homogenised modulus. For example, it is 58.22GPa and 57.33GPa from 3D and 1D modelling, respectively, for the 9mm model.

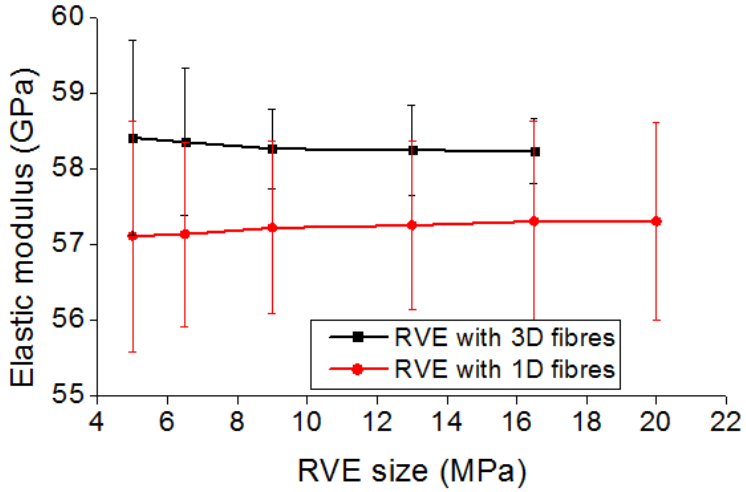

Fig .15 Size effect of RVE models on the predicted homogenised elastic modulus of UHPFRC

4.2.4 Comparison with experimental data and re-modelling

Table 4 compares the homogenised elastic moduli E_H of the mortar and the UHPFRC with the experimental data, where E_e is obtained from cylindrical compressive tests [2], E_u from ultrasonic pulse velocity tests and E_r from resonant frequency tests [57], respectively, all at 28 days. The differences between the homogenised results and the experimental data are shown in the brackets. It can be seen that the homogenised E_H=57.3GPa for the mortar overestimates the experimental E_e=42.08GPa by 36.17%, which in turn leads to 13.6~27.9% overestimations for the bulk of UHPFRC. There may be two reasons for this. The first is that the big pores with d_e >600μm, excluded in the first-scale homogenisation, may exist in the tested mortar specimens. The second may be the uncertainties involved in the micro-indentation tests, as reflected by the relatively high standard deviation in the moduli for the cement paste and the silica sand (see Table 2). Nano-indentation test can be carried out for more accurate results [23].

Table 4: Comparison of homogenised and experimental moduli using mean values of micro-indentation measurements

	E_H (GPa)	E_e (GPa)	E_u (GPa)	E_r (GPa)
Mortar	57.30	42.08 (36.2%)		
UHPFRC	58.26	45.55 (27.9%)	48.25 (20.8%)	51.3 (13.6%)

To clarify this issue, the lower bounds of the indentation results (computed by subtracting the standard deviation from the mean), E_s=74.61GPa for the silica sand and E_{cm}=44.33GPa for the cement paste, were used as inputs in the first scale. The homogenised elastic modulus of mortar matrix is 47.17GPa. This value was then used as input for the 9mm RVEs to be re-modelled, leading to E_H= 48.23±0.59 for the UHPFRC. The resultant differences with the experimental data now become very small, as summaries in Table 5.

Table 5: Comparison of homogenised and experimental moduli using low bounds of micro-indentation measurements

	E_H (GPa)	E_e (GPa)	E_u (GPa)	E_r (GPa)
Mortar	47.17	42.08 (11.56%)		
UHPFRC	48.23	45.55 (5.88%)	48.25 (-0.04%)	51.3 (-5.98%)

4.3 Effects of fibre volume fraction on homogenised moduli

As the usage of high-strength steel fibres is one of the main reasons for high cost of UHPFRC, the effects of fibre volume fraction were investigated. The 9mm RVE models with 1D fibre elements were re-simulated with f_f=6%, 8% and 10% in addition to the original 3.75%. The μXCT image-based meshes for the mortar with large pores were kept the same for all the models. A Matlab code was developed to randomly add more 1D fibre elements until the desired f_f was reached (see Fig. 16). To eliminate the effect of the fibre orientation, the newly added fibres had the same orientation factors with respect to the global axes as in the original models. The predicted elastic moduli were averaged over the five 9mm RVEs. The predicted E_H is 57.97, 58.28, and 59.02GPa for f_f=6%, 8% and 10%, respectively, with a slight increase over the 57.33GPa for f_f=3.75%. This indicates that the volume fraction of fibres randomly oriented does not significantly affect the elastic properties of UHPFRC as demonstrated by experiments [55, 56].

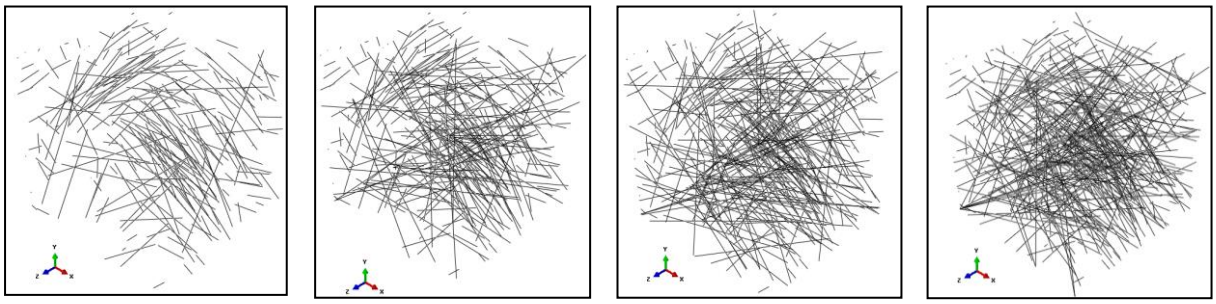

Fig .16 9mm RVE modelled with different fibre volume fractions: from left to right: 3.75%, 6%, 8% and 10%.

4.4 Effects of fibre orientation on homogenised moduli

The five 9mm RVE models with 1D fibre elements and f_f=10% were then simulated to study the effect of fibre orientation on the predicted E_H. All fibres were aligned with the x axis but placed randomly, so the fibre orientation factor η_i (Eq.1) with respect to x axis is 1 and close to zero with respect to other axes. The averaged elastic moduli are E_{11}=75.77GPa, E_{22}=56.57GPa and E_{33}=56.56GPa. E_{11} is about 34% higher than E_{22} and E_{33} and the anisotropy ratio for all the models is about 0.70, suggesting that the material is no longer isotropic. E_{11}=75.77GPa is about 28% higher than E_H=59.02GPa of the 9mm RVE models with the same f_f but randomly oriented fibres. This shows the significant effect of the fibre orientation on the elastic modulus of UHPFRC.

6. Conclusions

In this study, the 3D micro-structure of a 20mm UHPFRC cube with 150MPa compressive strength has been acquired by high-resolution μXCT scanning. The numbers, shapes, volume fractions and distributions of both steel fibres and pores are all visualised and determined by analysing the CT images with 24.8μm voxel resolution. It has been found in this specimen, there are over 12300 pores with size ranging from 25-1400 μm, among which 97.7% are smaller than 600 μm. This demonstrates the unrivalled capability of μXCT technique in revealing micro-structural details of composite materials like UHPFRC.

Based on the μXCT images and particularly the distribution of pore sizes, we have developed a two-scale homogenisation approach to calculate the effective elastic properties of UHPFRC. In the first (micro) scale, the sand particles, cement paste and the large number of small pores (<0.6mm), are analytically homogenised as the mortar matrix using the Mori-Tanaka method with the constituents' moduli obtained by micro-indentation tests. In the second scale, 3D meso-scale FE models of RVEs are built directly from the μXCT images for numerical homogenisation, with steel fibres and the small number of large pores (≥0.6mm) embedded in the homogenised mortar. The coupling of analytical and numerical homogenisation at different scales results in tremendous computational savings over other approaches using numerical homogenisation at both scales. The developed approach thus offers an accurate and efficient tool to conduct parametric studies for optimisation of the material's micro-structure for desired mechanical properties. The strength and fracture behaviour of UHPFRC at micro/meso-scales can also be predicted by nonlinear damage

mechanics models making use of the XCT images and the homogenised properties, which is an ongoing task.

Acknowledgements

The financial support from the Jordanian government (a 4-year full PhD studentship to Qsymah), the UK EPSRC (No. EP/J019763/1), and the US Air Force (EOARD grant No. FA8655-12-1-2100) is gratefully acknowledged.

References

1. Richard, P. and M. Cheyrezy, Composition of reactive powder concretes. Cement and Concrete Research, 1995. 25(7): p. 1501-1511.
2. Hassan, A., S. Jones, and G. Mahmud, Experimental test methods to determine the uniaxial tensile and compressive behaviour of ultra high performance fibre reinforced concrete (UHPFRC). Construction and Building Materials, 2012. 37: p. 874-882.
3. Mahmud, G.H., Z. Yang, and A.M. Hassan, Experimental and numerical studies of size effects of Ultra High Performance Steel Fibre Reinforced Concrete (UHPFRC) beams. Construction and Building Materials, 2013. 48: p. 1027-1034.
4. Millard, S., T. Molyneaux, S. Barnett, and X. Gao, Dynamic enhancement of blast-resistant ultra high performance fibre-reinforced concrete under flexural and shear loading. International Journal of Impact Engineering, 2010. 37(4): p. 405-413.
5. Mao, L., S. Barnett, D. Begg, G. Schleyer, and G. Wight, Numerical simulation of ultra high performance fibre reinforced concrete panel subjected to blast loading. International Journal of Impact Engineering, 2014. 64: p. 91-100.
6. Li, J., C. Wu, and H. Hao, An experimental and numerical study of reinforced ultra-high performance concrete slabs under blast loads. Materials & Design, 2015. 82: p. 64-76.
7. Walraven, J.C., High performance fiber reinforced concrete: progress in knowledge and design codes. Materials and Structures, 2009. 42(9): p. 1247-1260.
8. Le, T.T., Ultra high performance fibre reinforced concrete paving flags. 2008, University of Liverpool.
9. Yang, S., S. Millard, M. Soutsos, S. Barnett, and T. Le, Influence of aggregate and curing regime on the mechanical properties of ultra-high performance fibre reinforced concrete (UHPFRC). Construction and Building Materials, 2009. 23(6): p. 2291-2298.
10. Ezeldin, A.S. and P.N. Balaguru, Normal-and high-strength fiber-reinforced concrete under compression. Journal of Materials in Civil Engineering, 1992. 4(4): p. 415-429.
11. Alwan, J.M. and A.E. Naaman, New formulation for elastic modulus of fiber-reinforced, quasibrittle matrices. Journal of engineering mechanics, 1994. 120(11): p. 2443-2460.
12. Hill, R., The elastic behaviour of a crystalline aggregate. Proceedings of the Physical Society. Section A, 1952. 65(5): p. 349.
13. Hashin, Z. and S. Shtrikman, A variational approach to the theory of the elastic behaviour of multiphase materials. Journal of the Mechanics and Physics of Solids, 1963. 11(2): p. 127-140.
14. Eshelby, J.D., The determination of the elastic field of an ellipsoidal inclusion, and related problems. Proceedings of the Royal Society of London. Series A. Mathematical and Physical Sciences, 1957. 241(1226): p. 376-396.
15. Mori, T. and K. Tanaka, Average stress in matrix and average elastic energy of materials with misfitting inclusions. Acta metallurgica, 1973. 21(5): p. 571-574.
16. Benveniste, Y., A new approach to the application of Mori-Tanaka's theory in composite materials. Mechanics of materials, 1987. 6(2): p. 147-157.
17. Hill, R., A self-consistent mechanics of composite materials. Journal of the Mechanics and Physics of Solids, 1965. 13(4): p. 213-222.
18. Christensen, R. and K. Lo, Solutions for effective shear properties in three phase sphere and cylinder models. Journal of the Mechanics and Physics of Solids, 1979. 27(4): p. 315-330.

19. Constantinides, G. and F.-J. Ulm, The effect of two types of CSH on the elasticity of cement-based materials: Results from nanoindentation and micromechanical modeling. Cement and Concrete Research, 2004. 34(1): p. 67-80.
20. Ghabezloo, S., Association of macroscopic laboratory testing and micromechanics modelling for the evaluation of the poroelastic parameters of a hardened cement paste. Cement and Concrete Research, 2010. 40(8): p. 1197-1210.
21. Bernard, O., F.-J. Ulm, and E. Lemarchand, A multiscale micromechanics-hydration model for the early-age elastic properties of cement-based materials. Cement and Concrete Research, 2003. 33(9): p. 1293-1309.
22. Hemalatha, T., A. Ramaswamy, and J.C. Kishen, Micromechanical analysis of self compacting concrete. Materials and Structures, 2015. 48(11): p. 3719-3734.
23. Da Silva, W., J. Němeček, and P. Štemberk, Methodology for nanoindentation-assisted prediction of macroscale elastic properties of high performance cementitious composites. Cement and Concrete Composites, 2014. 45: p. 57-68.
24. Sorelli, L., G. Constantinides, F.-J. Ulm, and F. Toutlemonde, The nano-mechanical signature of ultra high performance concrete by statistical nanoindentation techniques. Cement and Concrete Research, 2008. 38(12): p. 1447-1456.
25. Zohdi, T.I. and P. Wriggers, An introduction to computational micromechanics. 1 ed. 2008: Springer Science & Business Media. 195.
26. Gal, E. and R. Kryvoruk, Meso-scale analysis of FRC using a two-step homogenization approach. Computers & Structures, 2011. 89(11): p. 921-929.
27. Zhang, J., X. Liu, Y. Yuan, and H. Mang, Multiscale modeling of the effect of the interfacial transition zone on the modulus of elasticity of fiber-reinforced fine concrete. Computational Mechanics, 2015. 55(1): p. 37-55.
28. Garboczi, E.J. and J.G. Berryman, Elastic moduli of a material containing composite inclusions: effective medium theory and finite element computations. Mechanics of materials, 2001. 33(8): p. 455-470.
29. Evans, L.M., L. Margetts, V. Casalegno, F. Leonard, T. Lowe, P. Lee, M. Schmidt, and P. Mummery, Thermal characterisation of ceramic/metal joining techniques for fusion applications using X-ray tomography. Fusion Engineering and Design, 2014. 89(6): p. 826-836.
30. Marrow, T., L. Babout, A. Jivkov, P. Wood, D. Engelberg, N. Stevens, P. Withers, and R. Newman, Three dimensional observations and modelling of intergranular stress corrosion cracking in austenitic stainless steel. Journal of Nuclear Materials, 2006. 352(1): p. 62-74.
31. Kerckhofs, G., J. Schrooten, T. Van Cleynenbreugel, S.V. Lomov, and M. Wevers, Validation of x-ray microfocus computed tomography as an imaging tool for porous structures. Review of Scientific Instruments, 2008. 79(1): p. 013711.
32. Pieritz, R.A., J.-B. Brzoska, F. Flin, B. Lesaffre, and C. Coléou, From snow X-ray microtomograph raw volume data to micromechanics modeling: first results. Annals of glaciology, 2004. 38(1): p. 52-58.
33. Mostafavi, M., N. Baimpas, E. Tarleton, R. Atwood, S. McDonald, A. Korsunsky, and T. Marrow, Three-dimensional crack observation, quantification and simulation in a quasi-brittle material. Acta Materialia, 2013. 61(16): p. 6276-6289.
34. Drummond, J.L., F. De Carlo, and B.J. Super, Three-dimensional tomography of composite fracture surfaces. Journal of Biomedical Materials Research Part B: Applied Biomaterials, 2005. 74(2): p. 669-675.
35. Song, I., D.N. Little, E.A. Masad, and R. Lytton, Comprehensive evaluation of damage in asphalt mastics using X-ray CT, continuum mechanics, and micromechanics (with discussion). Journal of the association of asphalt paving technologists, 2005. 74.
36. Ren, W., Z. Yang, R. Sharma, C. Zhang, and P.J. Withers, Two-dimensional X-ray CT image based meso-scale fracture modelling of concrete. Engineering Fracture Mechanics, 2015. 133(0): p. 24-39.
37. Garboczi, E.J., Three-dimensional mathematical analysis of particle shape using X-ray tomography and spherical harmonics: Application to aggregates used in concrete. Cement and Concrete Research, 2002. 32(10): p. 1621-1638.

38. de Wolski, S., J. Bolander, and E. Landis, An In-situ X-ray microtomography study of split cylinder fracture in cement-based materials. Experimental Mechanics, 2014. 54(7): p. 1227-1235.
39. Schell, J., M. Renggli, G. Van Lenthe, R. Müller, and P. Ermanni, Micro-computed tomography determination of glass fibre reinforced polymer meso-structure. Composites Science and Technology, 2006. 66(13): p. 2016-2022.
40. Sharma, R., P. Mahajan, and R.K. Mittal, Fiber bundle push-out test and image-based finite element simulation for 3D carbon/carbon composites. Carbon, 2012. 50(8): p. 2717-2725.
41. Barnett, S.J., J.-F. Lataste, T. Parry, S.G. Millard, and M.N. Soutsos, Assessment of fibre orientation in ultra high performance fibre reinforced concrete and its effect on flexural strength. Materials and Structures, 2010. 43(7): p. 1009-1023.
42. Suuronen, J.-P., A. Kallonen, M. Eik, J. Puttonen, R. Serimaa, and H. Herrmann, Analysis of short fibres orientation in steel fibre-reinforced concrete (SFRC) by X-ray tomography. Journal of Materials Science, 2012. 48(3): p. 1358-1367.
43. Ponikiewski, T., J. Katzer, M. Bugdol, and M. Rudzki, Steel fibre spacing in self-compacting concrete precast walls by X-ray computed tomography. Materials and Structures, 2015: p. 1-12.
44. Trainor, K.J., B.W. Foust, and E.N. Landis, Measurement of energy dissipation mechanisms in fracture of fiber-reinforced ultrahigh-strength cement-based composites. Journal of engineering mechanics, 2012. 139(7): p. 771-779.
45. Abrishambaf, A., J.A. Barros, and V.M. Cunha, Relation between fibre distribution and post-cracking behaviour in steel fibre reinforced self-compacting concrete panels. Cement and Concrete Research, 2013. 51: p. 57-66.
46. Kerschnitzki, M., P. Kollmannsberger, M. Burghammer, G.N. Duda, R. Weinkamer, W. Wagermaier, and P. Fratzl, Architecture of the osteocyte network correlates with bone material quality. Journal of bone and mineral research, 2013. 28(8): p. 1837-1845.
47. Yang, Q.-S. and Q.-H. Qin, Fiber interactions and effective elasto-plastic properties of short-fiber composites. Composite Structures, 2001. 54(4): p. 523-528.
48. Oliver, W.C. and G.M. Pharr, An improved technique for determining hardness and elastic modulus using load and displacement sensing indentation experiments. Journal of materials research, 1992. 7(06): p. 1564-1583.
49. Kanit, T., S. Forest, I. Galliet, V. Mounoury, and D. Jeulin, Determination of the size of the representative volume element for random composites: statistical and numerical approach. International journal of Solids and Structures, 2003. 40(13): p. 3647-3679.
50. Sharma, R., P. Mahajan, and R.K. Mittal, Elastic modulus of 3D carbon/carbon composite using image-based finite element simulations and experiments. Composite Structures, 2013. 98: 69-78.
51. Sun, C. and R. Vaidya, Prediction of composite properties from a representative volume element. Composites Science and Technology, 1996. 56(2): p. 171-179.
52. Pan, Y., L. Iorga, and A.A. Pelegri, Analysis of 3D random chopped fiber reinforced composites using FEM and random sequential adsorption. Computational Materials Science, 2008. 43(3): p. 450-461.
53. Damidot, D., K. Velez, and F. Sorrentino, Characterization of interstitial transition zone (ITZ) of high performance cement by nanoindentation technique. Proceeding of the 11th ICCC, Durban, South Africa, 2003: p. 314-323.
54. Kang, S.-T. and J.-K. Kim, The relation between fiber orientation and tensile behavior in an Ultra High Performance Fiber Reinforced Cementitious Composites (UHPFRCC). Cement and Concrete Research, 2011. 41(10): p. 1001-1014.
55. Köksal, F., F. Altun, İ. Yiğit, and Y. Şahin, Combined effect of silica fume and steel fiber on the mechanical properties of high strength concretes. Construction and Building Materials, 2008. 22(8): p. 1874-1880.
56. Thomas, J. and A. Ramaswamy, Mechanical properties of steel fiber-reinforced concrete. Journal of Materials in Civil Engineering, 2007. 19(5): 385-392.
57. Hassan, A. and S. Jones, Non-destructive testing of ultra high performance fibre reinforced concrete (UHPFRC): A feasibility study for using ultrasonic and resonant frequency testing techniques. Construction and Building Materials, 2012. 35: p. 361-367.